Fractal injectors to intensify liquid-phase processes by controlling the turbulent flow field

Shuxian Jiang[a], Jiajun Wang[a,*], Lian-Fang Feng[a], Marc-Olivier Coppens[b,*]

[a]*State Key Laboratory of Chemical Engineering, College of Chemical and Biological Engineering, Zhejiang University, Hangzhou 310027, PR China*

[b]*Centre for Nature Inspired Engineering & Department of Chemical Engineering, University College London, Torrington Place, WC1E 7JE London, UK*

* Corresponding author. *E-mail address*: jiajunwang@zju.edu.cn (Jiajun Wang), m.coppens@ucl.ac.uk (Marc-Olivier Coppens).

ABSTRACT

Fractal injectors can be used to intensify liquid-phase processes. The flow field, vortex structure and turbulent mixing performance induced by fractal injectors with three different fractal dimensions (D = 2, 2.58 and 3) are investigated. CFD simulations, using a renormalization group (RNG) k-ε turbulence model, are validated with particle image velocimetry (PIV) measurements. The structure and formation mechanism of the vortices are studied. Both spiral and double toroidal vortices are produced, the latter by jet impingement. These vortices interact with each other within a fractal generating unit. For the same total volumetric flow rate, a fractal injector with D = 2.58 can achieve better mixing uniformity than fractal injectors with D = 2 or D = 3, while maintaining a similarly high mixing rate to when D = 2. This is due to enhanced entrainment by mutually interacting double toroidal vortex pairs and turbulent mixing.

Keywords: fractal, injector, CFD, particle image velocimetry (PIV), vortex dynamics, turbulent mixing

Nomenclature

b	scaling ratio

c	clearance between the jet and the geometric center of multiple jets, m
c_1, c_2	length of horizontal tubes in generations 1 and 2, mm
c_i	molar concentration of species i in the reaction region, mol/m^3
$<c_i>$	average molar concentration of species i in the bulk fluid surrounding the reaction region, mol/m^3
$C_{A,0}$,	molar concentration of NaOH (A) in the jet fluid, mol/m^3
$C_{B,0}$, $C_{C,0}$	initial molar concentration of HCl (B) and $CH_2ClCOOC_2H_5$ (C) in the tank, mol/m^3
d_1, d_2	diameter of tubes in generations 1 and 2, mm
D	fractal (similarity) dimension
$D_{i,m}$	mass diffusion coefficient of species i, m^2/s
D_E	embedding dimension
D_t	turbulent diffusivity, m^2/s
D_T	topological dimension
E	engulfment parameter, 1/s
H	cylinder tank height, m
I	turbulent intensity
$\vec{J}_i$	diffusion flux of species i, kg/(m^2·s)
k	turbulence kinetic energy, m^2/s^2 or J/kg
k_1, k_2	second-order rate constant for reaction 1 and 2, m^3/mol·s
l_1, l_2	length of the vertical tubes in generations 1 and 2, mm
L	length of fractal line, m
m	number of similar parts in the fractal generator
$M_{w,i}$	molecular weight of species i, kg/mol
n	fractal generation number
n_E	total molar content of product E ($CH_2ClCOONa$), mol
N	number of tubes
N_c	number of cells

N_{outlet} number of injector outlets

r_i net production rate of species *i* by all reactions, mol/(m^3·s)

Re_j jet injection Reynolds number

R_i net production rate of species *i*, involving reactions and micromixing, kg/(m^3·s)

p pressure, Pa

Q total volumetric flow rate, m^3/h

s spacing between twin jets, m

S modulus of the mean rate-of-strain tensor, s^{-1}

Sc_t turbulent Schmidt number

S_i species *i* source term per unit mass due to the reaction, kg/(m^3·s)

S_{ij} rate-of-strain tensor, s^{-1}

t flow time, s

T cylinder tank inner diameter, m

$\vec{u}$ velocity vector, m/s

u_j jet injection velocity, m/s

U_x, U_y , U_z velocity in *x, y, z* direction, m/s

$\langle V_{eff} \rangle$ normalized effective reaction volume

V_m volume of cell *m*, m^3

V_{total} total effective volume of the vessel, m^3

w tracer mass fraction

w_{av} volume averaged tracer mass fraction

w_m tracer mass fraction in cell *m*

x, y, z Cartesian coordinates, m

Y_i mass fraction of species *i*

Greek Letters

δ scale or resolution, m

ε	turbulent dissipation rate, m^2/s^3
η	the ratio of the turbulent to mean strain time scale
μ	viscosity, kg/(m·s)
μ_t	turbulent viscosity, kg/(m·s)
ρ	density, kg/m^3
σ_w	standard deviation of the tracer mass fraction at time t
ω	vorticity, s^{-1}
Ω	normalized vorticity
Ω_n	normalized spanwise vorticity
Ω_s	normalized streamwise vorticity

1. Introduction

Fast reactions in the liquid phase are common in industry, such as in the production of polymers, fine chemicals, pharmaceutics or in biotechnology. Here, the mixing performance directly affects the production process. Mechanical mixing is one of the most common methods for fast liquid mixing, but in certain situations its use is limited. One example is the production of difluoromethane, where, due to the strongly corroding reactant, mixing is achieved by liquid phase injection. In other cases, fragile solid particles, such as cells, are suspended in the liquid and alternatives to mechanical mixing are desirable. Furthermore, the scalability of processes using impellers or spargers is not trivial when the reactions are transport limited and uniformity is important. Fractal injectors were invented about two decades ago as effective fluid distribution devices that aid scalability of the processes using them (Coppens, 2005). However, the impact of different fractal structures on liquid-liquid mixing has not been investigated before. As this article will show, this impact is non-trivial, presenting exciting opportunities to adjust the injector's fractal structure to improve mixing efficiency. First, self-similar fractals and the concept of fractal dimension are succinctly introduced, and previous research on the fractal engineering of fluid dynamics is briefly reviewed.

1.1 Self-similar fractals

Self-similar fractals are structures in which details look similar to the whole, under repeated magnification. This similarity can be exact or statistical, meaning that zooming in repeatedly on details reveals a statistically indistinguishable structure. Discovered by Benoit Mandelbrot, fractal geometry is universal in nature, and defies the conventions of classical Euclidean geometry and typical assumptions that depend on it, such as piecewise continuity of derivatives (Mandelbrot, 1983). Concepts like the length, L, of a curve or the area, S, of a surface no longer converge at increased resolution, but depend on the scale, δ, at which they are measured.

In mathematical fractals, this invariance under magnification may be repeated down to arbitrarily small scales, $\delta \to 0$, but, in nature, where fractals are abundant, scale-invariance only holds within a finite scaling range, $\delta_{\min} \le \delta \le \delta_{\max}$. This is the case for tree crowns and their bark, the branching airways of the lungs,

billowing clouds, lightning, porous bread, rugged mountains, natural coastlines, or the cascade of vortices in a turbulent mountain stream.

To quantify the space filling capacity of fractals, Mandelbrot introduced the fractal dimension, D, which is typically non-integer, and lies between the topological dimension, D_T, and the embedding dimension, D_E. Here, D_E is the integer dimension of the space the fractal is embedded in. The topological dimension is an integer as well: for points, $D_T = 0$, for lines, $D_T = 1$, and for surfaces, $D_T = 2$. Fractal lines have a dimension D in between 1 and D_E. For exact self-similar fractals, relevant to this article, the fractal dimension can be easily calculated as follows. Due to self-similarity, such a fractal can be considered built from m parts, each of which is similar to the whole, but a factor $1/b$ ($0 < b < 1$) smaller. In this case, $D = \log(m) / \log(1/b)$. A straight line can be considered to be constructed of m parts, $1/m$ times shorter, so $b = 1/m$ and $D = 1$, as expected. A square consists of $N = 4$ squares with an edge that is half as long as the original square, thus $b = 1/2$, and $D = \log4/\log2 = 2$; more generally, $m = 1/b^2$. However, for self-similar fractal lines, such as Koch curves, $m = 1/b^D$, and D is not necessarily an integer. At a resolution $\delta \sim b^n$, there are $N = m^n = b^{-nD} \sim \delta^{-D}$ equal segments, and the length of the fractal line thus depends on the scale δ as $L = N\delta \sim \delta^{1-D}$. Only when $D = 1$ does this value converge to a constant ("the" length) for $\delta \to 0$, but for fractal lines with $D > 1$, the length is scale dependent and would become infinite for the mathematical limit $\delta \to 0$. In practice, the number of generations, n, is finite. In the fractal injector described further on and shown in Figure 1, there are $N = 6$ parts that are $b = 1/2$ as long, and $D = \log6/\log2 \sim 2.58$, which is larger than 2 (more than area filling) and smaller than 3 (less than space filling). There exist other definitions for fractal dimensions that can be applied more broadly, such as the Hausdorff-Besicovitch and the box counting dimension, but, for exact self-similar fractals, all of these coincide with the similarity dimension. For more details, the reader is referred to (Mandelbrot, 1983) and (Coppens and Froment, 1995).

1.2 Fractal engineering of fluid dynamics

In engineering applications, fractal, self-similar branching structures may aid in the uniform and scalable distribution or collection of fluids (Coppens, 2005). A range of practical applications invokes fractal structures to affect the fluid dynamics. Such applications include fluid distribution, contacting and adsorption (Kearney,

1999; Kearney, 2000), gas-solid fluidized bed processes (Christensen et al., 2008a; Coppens, 2001; Coppens et al., 1999; Van Ommen et al., 2001), fluid mixers, multi-tubular heat exchangers (Luo et al., 2008; Tondeur and Luo, 2004), fuel cells and electrochemical devices (Kjelstrup et al., 2010; Trogadas et al., 2018; Trogadas and Coppens, 2020), noise reduction devices (Nedic et al., 2012) and other fluid-handling engineering apparatuses. A fractal structure, applied to the design of impeller blades, has been shown to lead to a smaller drag coefficient and lower power consumption compared with rectangular blades; the power number decreases with the number of fractal iterations, because the trailing vortices are broken up into smaller ones (Basbug et al., 2018; Steiros et al., 2017).

Kearney has described a three-dimensional fluid mixing device, which consists of a recursive structure of pipes; this structure is said to emulate turbulence using laminar flows (Kearney, 1999). In his principal design, each branch splits into 8 new branches, half the size, until an as small as possible size, to use as a "functional equivalence to turbulence", hence leading to mixing without turbulence. This concept could be attractive for a situation where the viscosity of the fluid in the vessel is very high, so that there is effectively very little turbulent mixing possible (Kearney, 2000). Theoretical approaches for the conception, modelling and design of fractal distributors have been developed as well. Bejan's "constructal" approach, based on irreversible thermodynamics to minimize entropy production, allows to design fractal distributors optimally, within certain constraints (Bejan, 2000). The basis of such optimization is a compromise between the "costs" related to pressure drop and viscous dissipation, on the one hand, and hold-up volume of the channel structure, on the other hand. The calculations lead to geometric scaling laws that relate the sizes of the channels at different branching levels of a fluid distributor (Tondeur and Luo, 2004).

Inspired by trees and lungs, Coppens introduced more general fractal injectors with $2 \leq D \leq 3$ (Coppens, 2001). Submerged in a bubbling gas-solid fluidized bed, the gas distributed through the fractal injector leads to "structuring" of the chaotic hydrodynamics and enhanced interphase mass transfer (Coppens, 2001; Coppens and van Ommen, 2003). Experimental results obtained in a lab-scale gas-solid fluidized bed indicate that the introduction of secondary gas via a fractal injector (with primary gas distributed through a bottom plate, to, at least, minimally fluidize the particles) improves mass transfer and gas-solid contact (Christensen

et al., 2008a; Christensen et al., 2008b; van Willigen et al., 2005). Such fractal injectors could also be used for other multiphase processes, as well as liquid-liquid mixing, which is the subject of this article.

Another way to use fractal structures to impact fluid dynamics is the use of fractal grids. Such grids can be used to increase the turbulent strain; instrumentation comprising hot-wire anemometry and particle image velocimetry (PIV) indicate that fractal grids increase the turbulent Reynolds number range compared to conventional perforated plate turbulence generators (Geipel et al., 2010). The turbulent field in fractal-generated turbulence is self-similar, and it has been found that the evolution of the flow generated by a fractal grid does not depend on the boundary conditions (Nagata et al., 2013; Weitemeyer et al., 2013). Fractal grids can generate much higher turbulence intensity than regular grids under the same inflow conditions and with similar blockage ratio, at the expense of a slightly larger pressure drop (Cafiero et al., 2014). Direct numerical simulations demonstrate that a fractal square grid is an efficient additional turbulence generator in the near-field region, where a fractal square grid can generate much higher turbulence levels and has a better mixing performance than a single square grid (Zhou et al., 2014). By analyzing the vortex structure, it can be found that, different from the well-known generation of spiral vortices due to the growth of azimuthal disturbances within the jet shear layer, a fractal grid introduces cross-wise disturbances, which produce streamwise vortices; these structures, although characterized by a lower energy content, have a deeper streamwise penetration than ring vortices, thus enhancing the entrainment process (Cafiero et al., 2015; Cafiero et al., 2016).

In contrast to fractal grids, the turbulent flow field around a fractal injector has not been studied yet. Fractal injectors of the type proposed by Kearney *et al.* mostly use laminar mixing. However, such fractal structures occupy a lot of space. They also ignore the importance of defining the smallest desired scale of the outlets, so that local mixing (which could be turbulent) around the outlets can be taken advantage of, which is much faster than laminar mixing. In this article, the flow field characteristics in a vessel equipped with fractal injectors are studied by means of computational fluid dynamics (CFD) simulations, which are validated by particle image velocimetry (PIV) measurements. The mixing performance of three fractal injectors with different fractal dimensions are compared in terms of the generated vortex structures and concentration field.

2. Experimental procedure

2.1 Experimental setup

The setup used for PIV experiments to validate the computer simulations is shown in Figure 1. The experiments were carried out using tap water (20 °C) in a flat bottom cylindrical tank, with inner diameter T = 0.093 m and height H = 0.208 m. A 0.2 m x 0.2 m x 0.2 m cubic tank enclosed the cylindrical tank to eliminate the effect of the cylindrical surface when conducting PIV experiments. Both the cylindrical tank and cubic tank were made of Perspex to enable full optical access for illumination and imaging. A two-generation, fractal injector with D = log6/log2 ~ 2.58 was fabricated in stainless steel by a form of additive manufacturing or 3D printing, called selective laser melting (SLM). The inner diameter of the nozzles was 3 mm. This fractal injector was located in the center of the water-filled tank. The injector was supplied via a water pump, and a flowmeter was used to control the total volumetric flow rate to 0.3 m^3/h, while the corresponding jet velocity, u_j = 0.33 m/s, and jet Reynolds number, Re_j = 1000. Water flew through the fractal injector to produce straight jets when exiting the outlets. Overflowing water from the tank re-entered the tank via the injector.

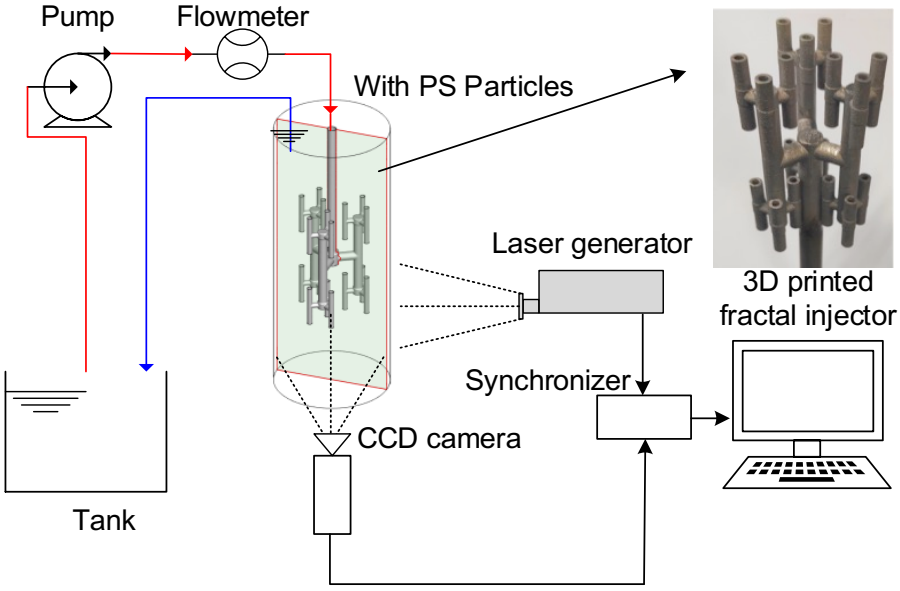

Fig. 1. Experimental setup for PIV measurements on the mixing of fluid (water with polystyrene (PS) particles as tracer) distributed through a fractal injector in a cubic tank containing water. A pump circulates overflowing water back into the tank via the fractal injector.

2.2 PIV measurements

The commercial two-dimensional (2D) PIV system (Dantec Dynamics A/S) used in the present study included a laser (New Wave Research Solo Nd:YAG, 200 mJ, 532 nm wavelength), a frame-straddling CCD camera (1600 × 1200 pixels), a synchronizer and DynamicStudio software (Dantec Dynamics A/S). This is schematically depicted in Figure 1. The spatial resolution was 0.6 × 0.8 mm^2. The flow was seeded with polystyrene (PS) particles (about 10 μm diameter) with a density of 1050 kg/m^3. The measured images were interrogated by 64 × 64 pixels windows with 75% overlap for both the *x* and the *z* direction. The time difference between laser pulses was set at 1000 μs, which was optimized to ensure that the maximum in-plane and out-of-plane displacements of the particles were less than one-quarter of the sizes of the interrogation windows and the thickness of the light sheet (Li et al., 2011). The spatial resolution of the velocity vectors was 0.6 × 0.8 mm^2. A cross-correlation algorithm was applied to obtain the instantaneous velocity distribution. Statistic independence of the mean velocities was verified: the difference between the mean velocity profiles calculated from 400 and 500 pairs was less than 1%, thus 400 pairs of images were captured in the various configurations.

3. Mathematical model

3.1 Constitutive equations

In order to simulate the turbulent mixing process in the fractal injector system, the governing equations include the mass conservation equation (continuity equation), Navier-Stokes equation and species conservation equations:

$$\frac{\partial \rho}{\partial t} + \nabla \cdot (\rho \vec{u}) = 0 \tag{1}$$

$$\rho\left(\frac{\partial \vec{u}}{\partial t} + \vec{u} \cdot \nabla \vec{u}\right) = -\nabla p + \nabla \cdot \left[\mu(\nabla \vec{u} + (\nabla \vec{u})^T)\right] \tag{2}$$

$$\frac{\partial (\rho Y_i)}{\partial t} + \vec{\nabla} \cdot (\rho \vec{u} Y_i) = -\vec{\nabla} \cdot \vec{J_i} + R_i + S_i \tag{3}$$

where ρ denotes the fluid density, t the flow time, $\vec{u}$ the velocity vector, p the pressure, Y_i and $\vec{J}_i$ the mass fraction and the diffusion flux of species i, respectively. R_i is the net rate of production of species i by chemical

reaction. S_i is the species source term per unit mass due to the reaction. In turbulent flow, the calculation of $\vec{J}_i$ is as follows:

$$\overrightarrow{J_i} = -(\rho D_{i,m} + \frac{\mu_t}{Sc_t})\nabla Y_i \tag{4}$$

where $D_{i,m}$ is the mass diffusion coefficient of species i, Sc_t is the turbulent Schmidt number. $Sc_t = \mu_t/(\rho D_t)$, μ_t and D_t are the turbulent viscosity and turbulent diffusivity, respectively.

3.2 Turbulence model

The renormalization group k-ε (RNG) model is based on the renormalization group analysis of the Navier-Stokes equations (Yakhot et al., 1992). Compared with the standard k-ε model (SKE), the RNG model includes the effect of rotation on turbulence and improves the prediction accuracy of rotational flow. Therefore, the RNG model is better adapted to the simulation of the flow at high strain rate, with a significant degree of streamline bending. The SKE model is suitable for fully developed turbulence, while, in the RNG model, the differential expression of the effective viscosity is obtained analytically, which can better simulate the flow at low Reynolds number. Here, k and ε satisfy:

$$\frac{\partial}{\partial t}(\rho k) + \nabla \cdot (\rho k \vec{u}) = \nabla \cdot [(\mu + \frac{\mu_t}{\sigma_k})\nabla k] + P_k - \rho\varepsilon \tag{4}$$

$$\frac{\partial}{\partial t}(\rho \varepsilon) + \nabla \cdot (\rho \varepsilon \vec{u}) = \nabla \cdot [(\mu + \frac{\mu_t}{\sigma_\varepsilon})\nabla \varepsilon] - \frac{C_{\varepsilon 1}\varepsilon}{k} P_k - C_{\varepsilon 2}^* \rho \frac{\varepsilon^2}{k} \tag{5}$$

where

$$P_k = \mu_t S^2 \tag{6}$$

and the modified coefficients are

$$C_{\varepsilon 2}^* = C_{\varepsilon 2} + \frac{C_\mu \eta^3 (1 - \eta/\eta_0)}{1 + \beta \eta^3} \tag{7}$$

where $\eta = Sk/\varepsilon$ and S is the modulus of the mean rate-of-strain tensor with elements S_{ij}: $S = (2S_{ij}S_{ij})^{1/2}$. In the RNG model, the following values for the closure coefficients are used: $C_\mu = 0.0845$, $\sigma_k = 0.7194$, $\sigma_\varepsilon = 0.7194$, $C_{\varepsilon 1} = 1.42$, $C_{\varepsilon 2} = 1.68$, $\eta_0 = 4.38$, and $\beta = 0.012$.

3.3 Quantification of the degree of mixing

The mechanism of turbulent mixing is complicated. Mixing plays a crucial role for fast reacting systems. According to the turbulence scale, the mixing process can be characterized by macro-, meso- and micro-mixing. Macro-mixing is carried out in the whole reactor, which determines the environmental concentration of meso-mixing and micro-mixing, as well as transfers the fluid in the process of micro-mixing and meso-mixing (Schwertfirm et al., 2007). Meso-mixing is related to the inertial-convective mixing process, which reflects the turbulent transfer process between the fresh material and the ambient fluid on intermediate scales. Turbulent micro-mixing is determined by the effect of fluid element deformation on the acceleration of molecular diffusion, engulfing of the environment, inertial-convective disintegration of large eddies and local intermittency (Bałdyga and Pohorecki, 1995).

The tracer concentration distribution obtained by the numerical simulations in this paper can only qualitatively evaluate the macro-mixing performance. Therefore, it is necessary to calculate the mixing performance as a way to quantitatively compare different injectors. The volume-averaged tracer mass fraction w_{av} at any time t can be defined as follows (Kockmann et al., 2003):

$$w_{av} = \frac{\sum_{m=1}^{N_c} V_m w_m}{\sum_{m=1}^{N_c} V_m} = \frac{\sum_{m=1}^{N_c} V_m w_m}{V_{total}} \tag{8}$$

where w_m is the tracer mass fraction in cell m, V_m is the cell volume, V_{total} is the total effective volume of the vessel (the volume occupied by the injector is not considered), and N_c is the number of cells. The standard deviation of the tracer mass fraction at time t, σ_w, is defined by:

$$\sigma_w = \sqrt{\frac{\sum_{m=1}^{N_c} V_m (w_m - w_{av})^2}{V_{total}}} \tag{9}$$

The smaller σ_w, the better the mixing uniformity.

The parallel competitive reaction system proposed by Yu is employed to probe the micro-mixing (Yu, 1993). The fast reaction of the competitive reactions is the neutralization of sodium hydroxide:

$$NaOH(A) + HCl(B) \xrightarrow{k_1} H_2O + NaCl(D) \quad (10)$$

with a second-order rate constant $k_1 = 1.3 \times 10^8$ m^3/mol·s (25 °C), while the slow reaction is the hydrolysis of ethyl chloroacetate:

$$NaOH(A) + CH_2ClCOOC_2H_5(C) \xrightarrow{k_2} CH_2ClCOONa(E) + C_2H_5OH(F) \quad (11)$$

with a second-order rate constant $k_2 = 0.034$ m^3/mol·s (25 °C).

The Finite Rate (FR) / Eddy Dissipation (ED) model is adopted to describe the volumetric parallel competitive reactions. It considers the effects of both the reaction kinetics and the turbulent flow on the reaction process (Han et al., 2012). On this basis, the standard *E* model is introduced to describe unsteady micro-mixing and diffusion in the deforming laminated structures formed by turbulent entrainment (Baldyga and Bourne, 1984). The net rate of production of species *i*, affected by micro-mixing, is calculated by the following equation:

$$R_i = M_{w,i}[E(< c_i > - c_i) + r_i] \quad (12)$$

where $M_{w,i}$ denotes the molecular weight of species *i*, c_i is the molar concentration of species *i* in the reaction region, $<c_i>$ is the average molar concentration of species *i* in the bulk fluid surrounding the reaction region, and r_i is the net rate of formation of species *i*. The engulfment parameter *E* is defined as the rate of micromixing:

$$E = 0.058(\frac{\rho\varepsilon}{\mu})^{1/2} \quad (13)$$

Initially, the tank was filled with HCl solution (B) and $CH_2ClCOOC_2H_5$ solution (C), each with a concentration of 70 mol/m^3: $C_{B,0} = C_{C,0} = 70$ mol/m^3. At $t = 0$, NaOH solution with a concentration $C_{A,0} = 73.5$ mol/m^3 was injected into the tank through the nozzles of the fractal injector. The injection was stopped at $t = 0.05$ s.

3.4 Simulated systems

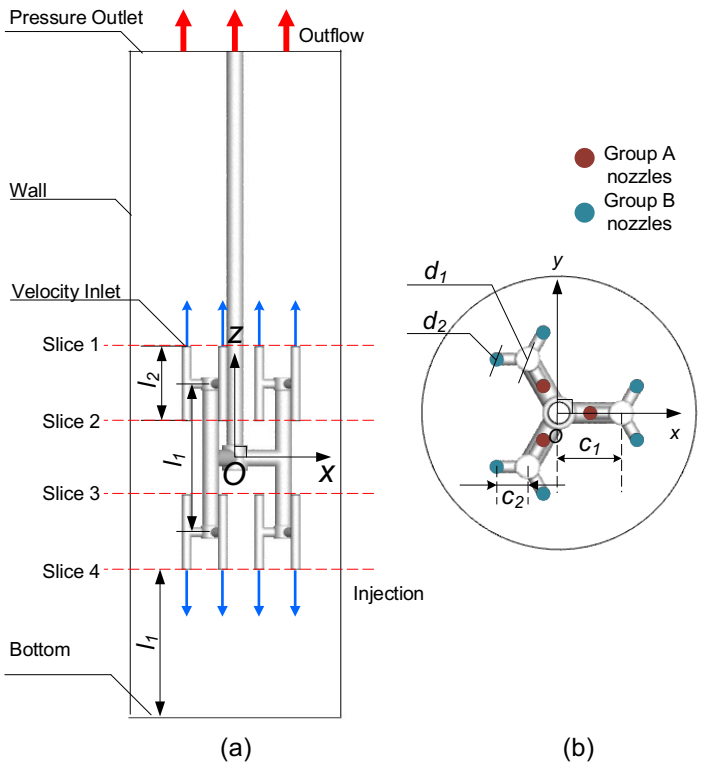

Fig. 2. (a) Schematic illustration of the simulation setup for a second-generation fractal injector with D = 2.58; (b) magnification of the fractal injector, introducing the two groups of nozzles (A: closer to the center, B: further away from the center), the four horizontal slices containing the nozzles, the horizontal (c_n) and vertical (l_n) pipe lengths and diameters (d_n) within the first and second generation of the injector (n = 1, 2).

The previously introduced fractal injector is schematically shown in Fig. 2. The tube network of the fractal injector has a recursive structure, in which different generations of tubes, n, can be distinguished. The child generation (n = 2) is substantially similar in geometry to the tubes of the corresponding parent generation (n = 1) from which it is branching. A vertical central tube divides into 3 tubes, branching out horizontally with their endpoints on an equilateral triangle. The endpoint of each tube branches upward and downward into another vertical tube. This generating unit is repeated through a self-similar cascade; higher numbers of generations could be achieved, but they are not considered here.

Considering that the flow in a child generation can be regarded as submerged parallel jets, the behavior of a child generation can be identified through the relationship between the flow field structure and geometric parameters of submerged parallel liquid jets from our previous work (Jiang et al., 2020). The diameter of the

child generation tubes, d_2 = 3 mm, the length of the horizontal tubes, $c_2 = 2.5d_2$, and the length of the vertical tubes, $l_2 = 7.715d_2$. Compared to the parent, the pipe length of a child generation is halved, with a scaling ratio $b = l_2/l_1 = c_2/c_1 = 0.5$. The parameters of the 2nd generation are such that the vertical distance between two adjacent tubes equals the characteristic length of submerged parallel jets, which is the length from the nozzles to the combine point of parallel jets (Jiang et al., 2020). The nozzles are distributed on four different horizontal planes, marked as slices 1, 2, 3 and 4, from top to bottom, and the distance from the bottom of the vessel to slice 4 equals l_1. Nozzles can be divided into groups A and B, according to the distance between the center of a nozzle and the center of vessel, where group A nozzles are closer to the center and the distance from it is (c_1-c_2). The Cartesian frame of reference has its origin located at the center of the fractal injector.

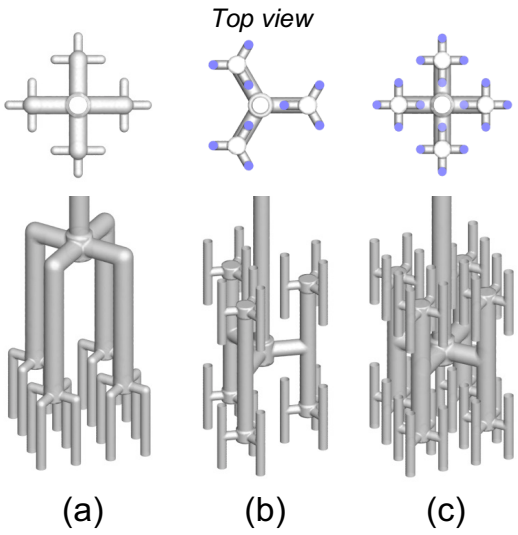

Fig. 3. Fractal injectors with (a) D = 2, N_{outlet} = 16; (b) D = 2.58, N_{outlet} = 36; (c) D = 3, N_{outlet} = 64.

In this paper, two other fractal injectors of different morphology are also studied for comparison (Figs. 3a and 3c). The difference between these three cases is the number m of child generations produced by each parent iteration, while b = 0.5 in each case. In Fig. 3a, the parent generation branches into 4 channels with their endpoints on a square, and each tube descends into another vertical tube, thus m = 4 and D = log4/log2 = 2. In Fig. 3c, each of the four horizontal tubes splits into descending and ascending vertical tubes, leading to m = 8 and D = log8/log2 = 3. These two cases could be considered two extreme cases of fractal injector, where D = 2 is a planar structure, like a classic fluid distributor, and D = 3 is a volume-filling structure.

The total volumetric flowrate is controlled to be the same for these three cases: Q = 0.916 m^3/h. The injection velocity and injection Reynolds number for case D = 2 are u_j = 2.25 m/s and Re_j = 6750, respectively; for case D = 2.58, they are u_j = 1.00 m/s and Re_j = 3000; and for case D = 3, u_j = 0.5625m/s and Re_j = 1687.5.

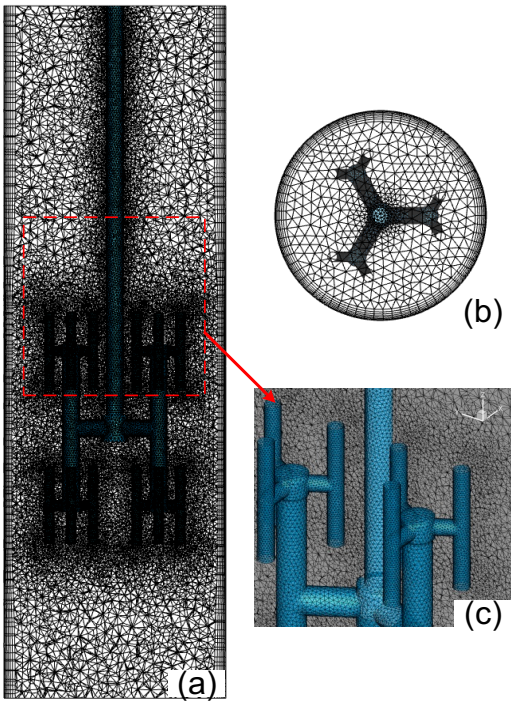

Fig. 4. Computational grid in (a) central vertical plane; (b) top view; (c) close-up of the region around a nozzle.

The geometrical objects and simulation grids were created with Gambit 2.4.6 (ANSYS Inc.). The employed unstructured grid is shown schematically in Fig. 4. Tetrahedral cells were used for the computational domain. The grid became finer in the regions near each nozzle. A boundary layer was added near the wall of the vessel. To obtain mesh-independent solutions, tests were conducted using three different sets of grids. Fig. 5 shows the vertical velocity profile for a D = 2.58 fractal injector with three different average mesh sizes; it can be seen that the domain with an average mesh size of 3 mm (2,149,094 cells) has a vertical velocity profile that is very close to the result using an average mesh size of 2.5 mm (2,782,075 cells), but deviations using a mesh size of 4 mm are quite substantial. Therefore, in subsequent simulations, an average mesh size of 3 mm was chosen, as a compromise between calculation speed and accuracy.

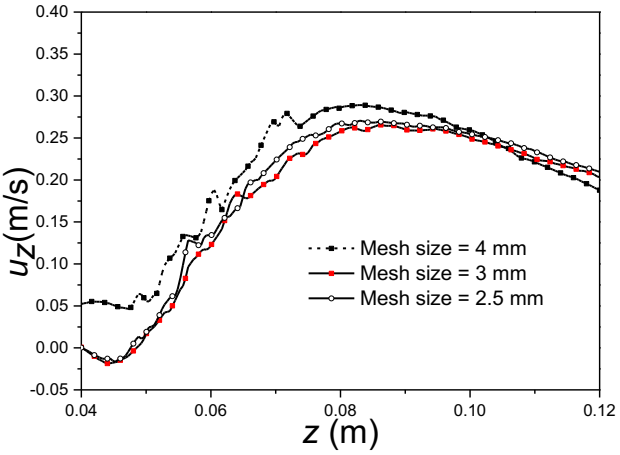

Fig. 5. Vertical velocity profile for grid-independence check (Re_j = 3000, D = 2.58, at line x = 0.015, y = 0).

The simulations were carried out using the commercial software package ANSYS Fluent 19.2. All the injection nozzles were specified as velocity inlet boundaries. A pressure outlet boundary condition was applied at the top surface of the vessel. No-slip boundary conditions were applied at the walls of the vessel and the fractal injector. The governing equations for conservation of momentum, pressure and turbulence characteristics were solved using the steady-state, segregated pressure-based solver. The SIMPLEC algorithm for pressure-velocity coupling was adopted. A second-order upwind scheme was used for spatial discretization of the equations. Water at 25 °C was used as the working fluid (ρ = 997.8 kg/m^3 and μ = 0.00089 Pa·s).

After simulating the steady-state flow field, unsteady simulations of the species transport equation were carried out to study the mixing process. The time t = 0 s corresponds to the injection time of the tracer into the tank. A time step of 0.005 s was used to advance the simulation clock. Convergence was assumed when the residuals for all governing equations reached a value below 10^{-6}. Calculations were stopped when t = 1.0 s. The tracer was assigned the physical properties of water, expect for a diffusion coefficient of 10^{-10} m^2/s.

4. Results and discussions

4.1 Validation of the CFD simulation method

CFD simulation results were validated by computing the vertical velocity profiles by the RNG turbulent model and comparing the values to those obtained experimentally from PIV data. Fig. 6 shows that the RNG

turbulent model is in satisfactory agreement with PIV experimental data. In our previous work (Jiang et al., 2020), a comparison between the calculated and PIV experimental results also indicated that the RNG turbulence model could satisfactorily predict the hydrodynamic flow field of submerged, parallel liquid jets at Re_j = 3000. Thus, it was deemed reasonable to adopt the RNG turbulent model for this paper.

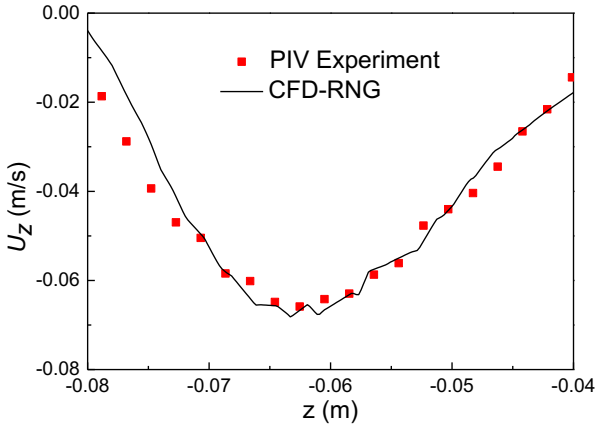

Fig. 6. Vertical velocity profiles, comparing CFD results with PIV data along the vertical line through $x = 0$, $y = 0$ (Re_j = 1000, D = 2.58, d_2 = 3 mm, for water at 20 °C).

4.2 Hydrodynamics and vortex dynamics of fractal injector (D = 2.58)

The flow field and turbulence kinetic energy of the fractal injector are shown in Fig. 7. Vertical slices A-A' and B-B' represent vertical sections passing through a pair of group A nozzles and group B nozzles, respectively. The velocity u is normalized by the injection velocity u_j, $\langle U \rangle = u/u_j$.

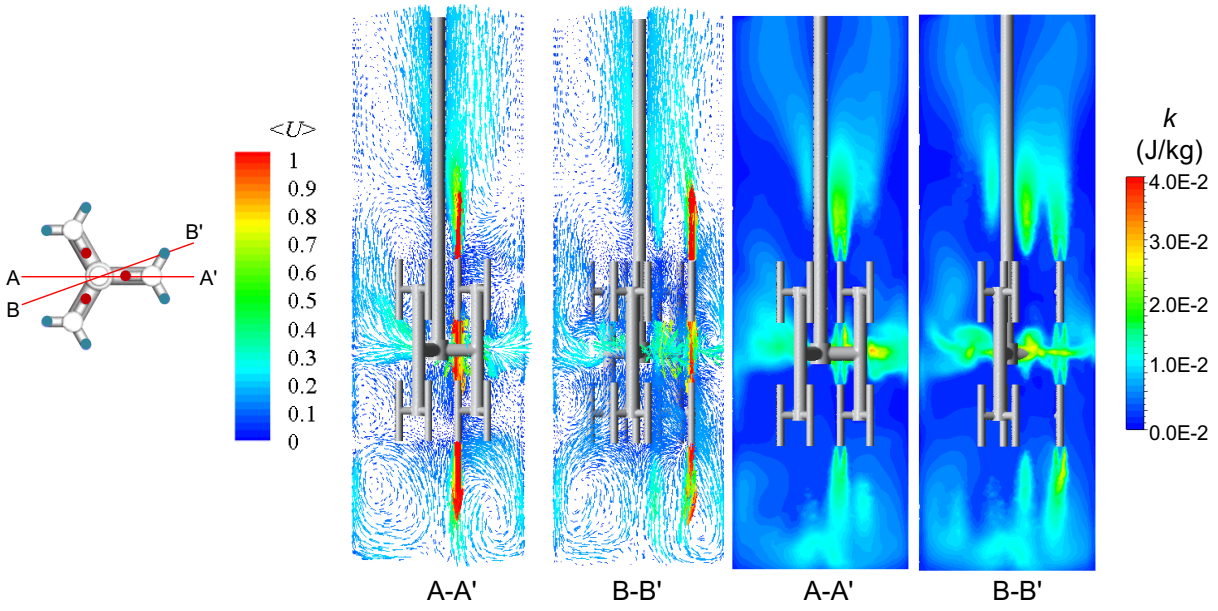

Fig. 7. Normalized velocity vector field ($<U> = u/u_j$) and turbulence kinetic energy (k) contours in two vertical slices A-A' and B-B' ($Re_j = 3000$, $D = 2.58$, $d_2 = 3$ mm).

As can be seen from Fig. 7, for the highest nozzles, distributed on slice 1, multiple jets are merged after a period of development, and the turbulence kinetic energy is mainly concentrated in the developmental stage of multiple jets. For the vertically central nozzles, distributed within slices 2 and 3, due to the obstruction of the horizontal tubes, the jets in group A do not collide directly, and the direction of flow is changed sharply around the curved surface of the horizontal tube. The turbulence kinetic energy near the central region is mainly generated by the normal strain in the impinging process. Two asymmetric radial jets are formed after the impinging of opposite jets; then, the jets impact the vessel wall, the streamlines bend again, upward and downward flows are formed along the wall, and two weak circulation zones are generated at the same time. For group B, the jets of slice 2 and slice 3 impact each other directly, and the turbulence kinetic energy reaches its maximum value. After the bending of jet streamlines, the radial jet on one side forms many smaller vortices around the tube due to the obstruction by the fractal injector's tubes. For the nozzles on the bottom slice 4, the downward multiple jets impact the bottom wall due to obstruction by the bottom wall. At the stagnation point, the streamlines bend and move along the radial direction. A circulation zone appears near the bottom of the vessel.

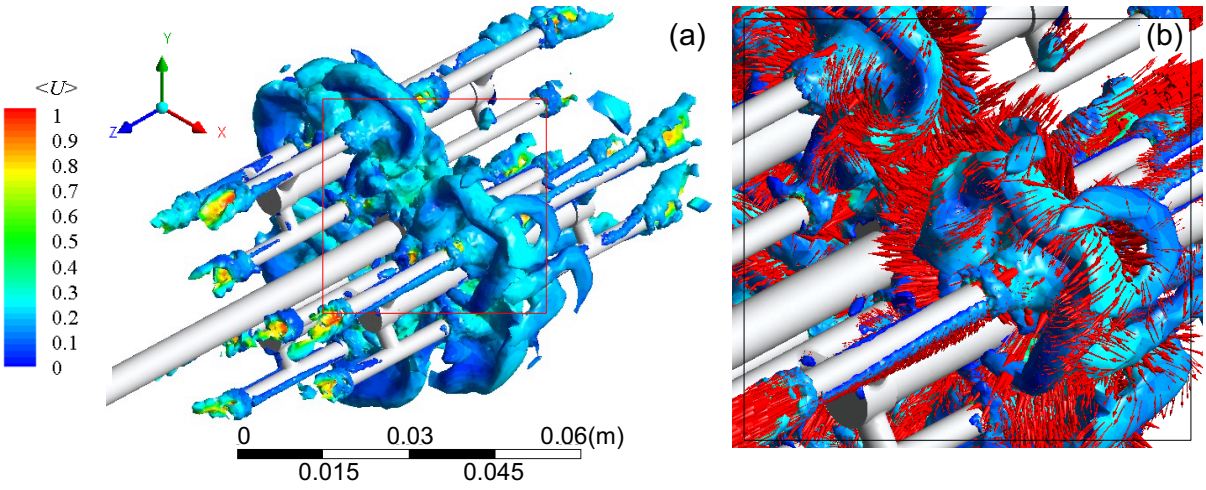

Fig. 8. (a) Isosurface of vorticity at $\Omega = \omega d_2/u_j = 0.09$, colored by normalized velocity $<U> = u/u_j$; (b) Local amplification of isosurface of vorticity overlaid with velocity vector ($Re_j = 3000$, $D = 2.58$, $d_2 = 3$ mm).

Fig. 8 illustrates the vortices generated by the fractal injector jets. The distinct spiral vortices cannot be observed near a nozzle in slice 1, because there is less interference in this region. For slice 4, the downward jets will impact the bottom wall, and the movement and deformation of the vortex ring will rapidly develop into a single spiral vortex. For the region between slices 2 and 3, considering the complexity of the flow, Fig. 8b is obtained after enlarging the vortices' isosurface, with the velocity vector field overlaid on the isosurface. It can be seen that a double toroidal vortex structure is formed. The sizes of the upper and lower vortex rings are different, while the diameter of the vortex ring near slice 2 is larger than that near slice 3. The adjacent groups of impinging jets are connected by the vortex tubes.

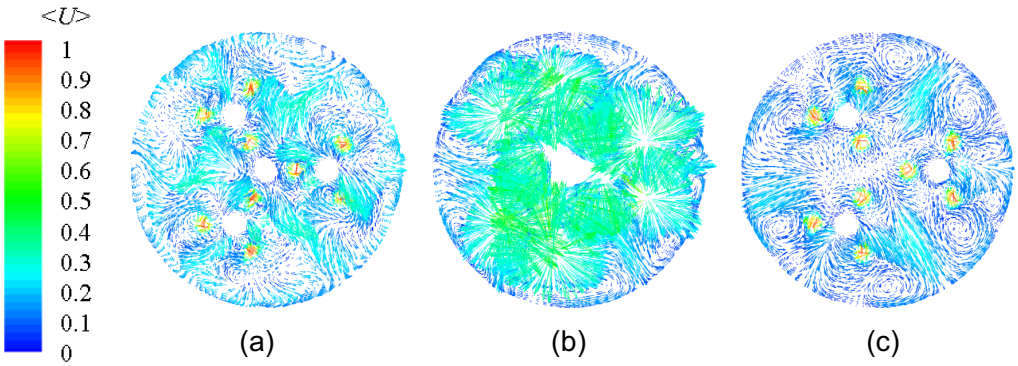

Fig. 9. Normalized velocity vectors in three horizontal slices: (a) $z = 1.93d_2$; (b) $z = 0$; (c) $z = -1.93d_2$ (Re_j = 3000, D = 2.58, d_2 = 3 mm).

In order to further investigate the vortex structure in this region, the velocity vectors for $z = -1.93d_2$, 0 and $1.93d_2$ are shown in Fig. 9. It can be seen that the radial velocity component for $z = 1.93d_2$ is significantly larger than that for $z = -1.93d_2$, which is consistent with the larger upper toroidal vortex observed in Fig. 8. Obvious interaction between the three jets located in the same fractal unit can be observed in Fig. 9a, but it is not apparent for $z = -1.93d_2$ in Fig. 9c. The cross-section $z = 0$ is the plane where the collision takes place, and the radial component of the velocity reaches its maximum.

The vortex structure between slices 2 and 3 is summarized in Fig. 10. After the collision between downward and upward jets, two vortex rings rotating in opposite directions are formed. The inner side of the upper vortex

ring interacts with the outer side of the lower vortex rings. The diameter of the upper vortex ring is larger, because it is also affected by the adjacent pairs of double toroidal vortices.

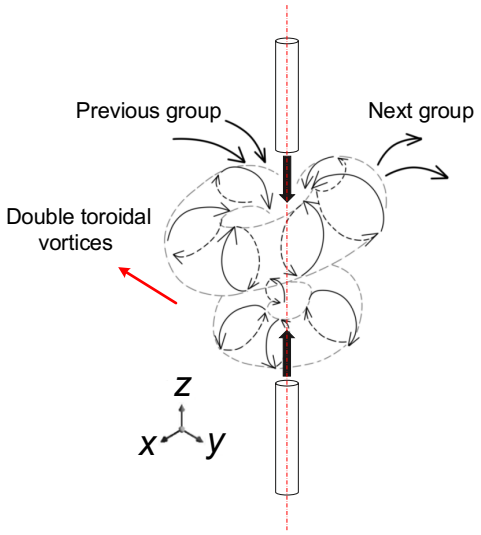

Fig. 10. Schematic of the vortices formed between the nozzles lying in slices 2 and 3.

The streamwise vortices are generated through the development of a turbulent boundary layer, which plays an important role in the entrainment of the jets. The vortices stretch along the flow direction, then break down and gradually develop to the inner and outer sides of the jet to form the mixing layer (Xu et al., 2020). The spanwise vortices are generated by the velocity gradients of the jet flow and the ambient fluid (Lasheras et al., 1986). Driven by the viscous shear force, the spanwise vortices are wound along the edge of the geometric structure of the device. The distribution of the spanwise vortices is relatively regular, especially in the region near a nozzle, as it is constrained by the spatial environment of each nozzle. The normalized streamwise vorticity (STV) is defined as follows(Hu et al., 2002):

$$\Omega_s = \frac{d}{u_j}\left(\frac{\partial U_y}{\partial x} - \frac{\partial U_x}{\partial y}\right) \tag{14}$$

and the normalized spanwise vorticity (SPV) is defined as follows:

$$\Omega_n = \frac{d}{u_j}\sqrt{\left(\frac{\partial U_z}{\partial y} - \frac{\partial U_y}{\partial z}\right)^2 + \left(\frac{\partial U_x}{\partial z} - \frac{\partial U_z}{\partial x}\right)^2} \tag{15}$$

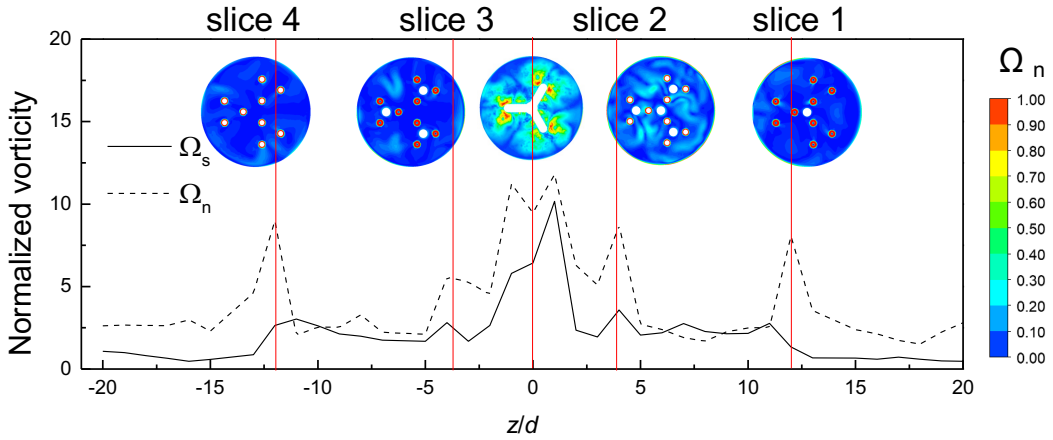

Fig. 11. Peak value variation of streamwise (Ω_s) and spanwise (Ω_n) vorticity, and the contours of Ω_n (Re_j = 3000, D = 2.58, d_2 = 3 mm).

The physical properties of liquids are quite different from those of gases, and the turbulent eddy structures decay rapidly in the flow process, which is conducive to the mutual entrainment and mixing of the jet and the surrounding fluid (Luo et al., 2016). The peak value variation of the spanwise and the streamwise vorticity along the axis are shown in Fig. 11, and the five spanwise vorticity contours refer to slices 1, 2, 3, 4 and the horizontal cross-section at z = 0. There is a correspondence between the distributions of the regions of high turbulence kinetic energy and high vorticity. In particular, it can be seen that the peaks in streamwise vorticity are concentrated in the region between slice 2 and slice 3 ($-3.8575 < z/d < 3.8575$), where the turbulence kinetic energy reaches a maximum (Fig. 7). The peak value of the streamwise vorticity decays fastest in this region, which indicates that the turbulent vortices break down rapidly and the entrainment and turbulent mixing are enhanced in the region near to the jets (Liepmann and Gharib, 1992; Toyoda and Hiramoto, 2006). It can be observed in the Ω_n contours (Fig. 11) that there are more intense and more uniform vortices in the region where jets collide; the average spanwise vorticity in slice 2 is larger than that in slice 3, because the flow rate through slice 2 is larger than that through slice 3, and there are more variations in the entrainment field, which might enhance the evolution of the secondary, three-dimensional vortex structures (Liepmann and Gharib, 1992). The spanwise vortices are obviously affected by the spatial distribution of the nozzles (Xu et al., 2020), and the vorticity peaks can be found near the planes in which the nozzles are located, as well as in the plane where the jets impinge with each other (z = 0).

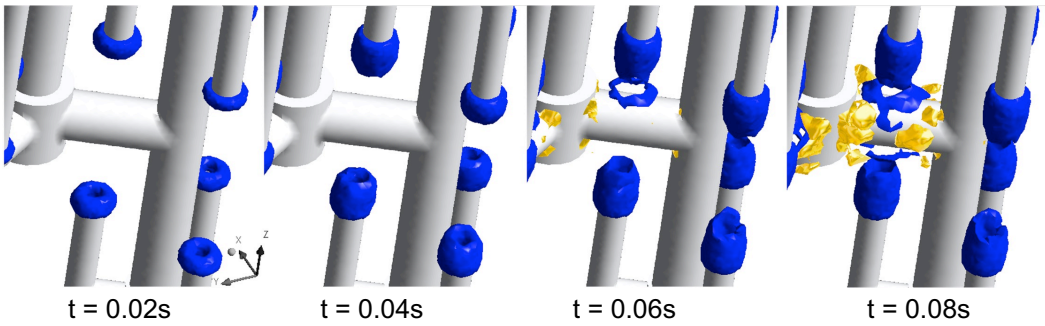

Fig. 12. Instantaneous flow field features for the fractal injector; isosurface of normalized spanwise vorticity $\Omega_n = 1.0$ (blue) and of normalized streamwise vorticity $\Omega_s = 0.3$ (yellow) ($Re_j = 3000$, $D = 2.58$, $d_2 = 3$ mm).

Fig. 12 provides further visual information on the evolution of the spanwise and streamwise vortices between slices 2 and 3. Spanwise vortices develop rapidly from the perimeter of the orifices, and they are stretched along the z axis, along with the development of the jets. When the two jets begin to impact each other, the spanwise vortices become unstable and are fragmented (at $t = 0.06$ s), increasing in diameter. Superimposed on the primary spanwise vortex structure, there is a secondary streamwise vortex structure (Bernal and Roshko, 1986). The streamwise vortices are generated on the periphery of the impacting face.

4.3 Hydrodynamics of three fractal injectors

The normalized velocity contours are reported in Fig. 13. The main differences between the two cases where $D = 2.58$ and $D = 3$, in which the nozzles are spatially distributed (rather than just in a horizontal plane), can be spotted in the vicinity of the impinging cross-section, between slices 2 and 3.

The flow field of the case where $D = 3$ can be characterized by symmetry in the collision region. Since the nozzles are axisymmetrically distributed, the radial jets formed after the collision are affected by the stream moving upward from the bottom with the same flow rate. In the vicinity of the side wall, the radial jets change direction and flow upward.

On the other hand, for the case where $D = 2.58$, the nozzles are asymmetrically distributed. The radial jets formed after collision are weakly affected by the flow moving upward, and, after encountering the side wall, jets which move both upward and downward along the wall are formed. Also, for the case where $D = 3$, the

streamlines of the jets bend more strongly than for the case where $D = 2.58$. Therefore, the streamlines merge earlier.

For $D = 2$, the nozzles are distributed within one plane (slice 4). After the multiple jets impinge on the bottom wall, the flow changes direction and forms upward wall jets. Because the flow rate is the same and there are less nozzles, Re_j is larger than for the other two cases, and turbulence near the nozzles is more intense.

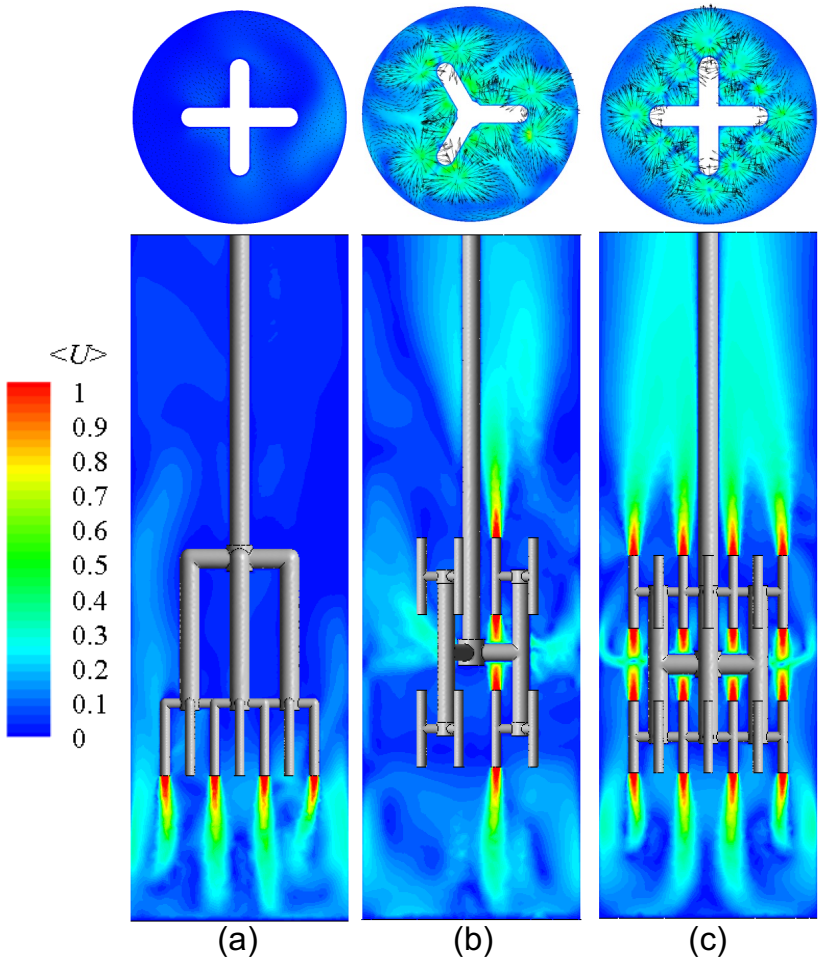

Fig. 13. Normalized velocity contours (<*U*>) in the $y = 0$ vertical plane and the $z = 0$ horizontal slice for fractal injectors with (a) $D = 2$, (b) $D = 2.58$, and (c) $D = 3$ ($Q = 0.916$ m^3/h, $d_2 = 3$ mm).

The isosurface of the vorticity at $\Omega = 30$ s^{-1} is shown in Fig. 14. Comparing the case where $D = 3$ to $D = 2.58$, the vortices in the jet collision region are smaller and the diameters of the upper- and lower-layer vortex rings differ less. In addition, adjoining double toroidal vortices interact less vigorously for $D = 3$ than for $D = 2.58$. For the regions near slices 1 and 4, the spiral vortices deform and break up rapidly around the nozzles. For $D = 3$, the injection velocity and associated Reynolds number ($Re_j = 1687.5$) is lowest for the same flow

rate, which creates the weakest turbulence. For $D = 2$, due to the highest injection velocity and, thus, the most intense turbulence, all jets impact the wall at the same time, and a large vortex tube is formed around the wall.

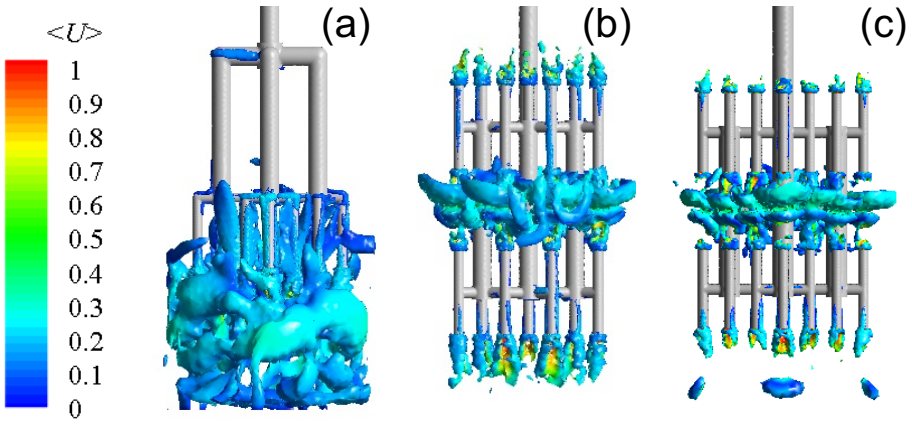

Fig. 14. Isosurface of vorticity at $\Omega = 30\ s^{-1}$, colored by the normalized velocity, $<U>$, and represented for fractal injectors with (a) $D = 2$, (b) $D = 2.58$, and (c) $D = 3$ ($Q = 0.916\ m^3/h$, $d_2 = 3$ mm).

The distribution and decay of the normalized streamwise and spanwise vorticity along the axial direction can be observed in Fig. 15.

For $D = 2$, the peak value of Ω_n is less than that of Ω_s, and the maximum values for Ω_n and Ω_s appear in the region near the bottom wall, where turbulence is most intense. When impinging on the wall, the jets deflect strongly and dissipate energy rapidly. Subsequently, the peak values of Ω_n and Ω_s decay rapidly.

For $D = 3$, the distribution of Ω_s is close to that for $D = 2.58$, while there is a significant difference in Ω_n. There is no obvious relationship between the peak location of Ω_n and the nozzle distribution. Spanwise vortices are concentrated in the jets' collision region. Compared with the other two cases, the spanwise vorticity, Ω_n, is much larger when $D = 2.58$.

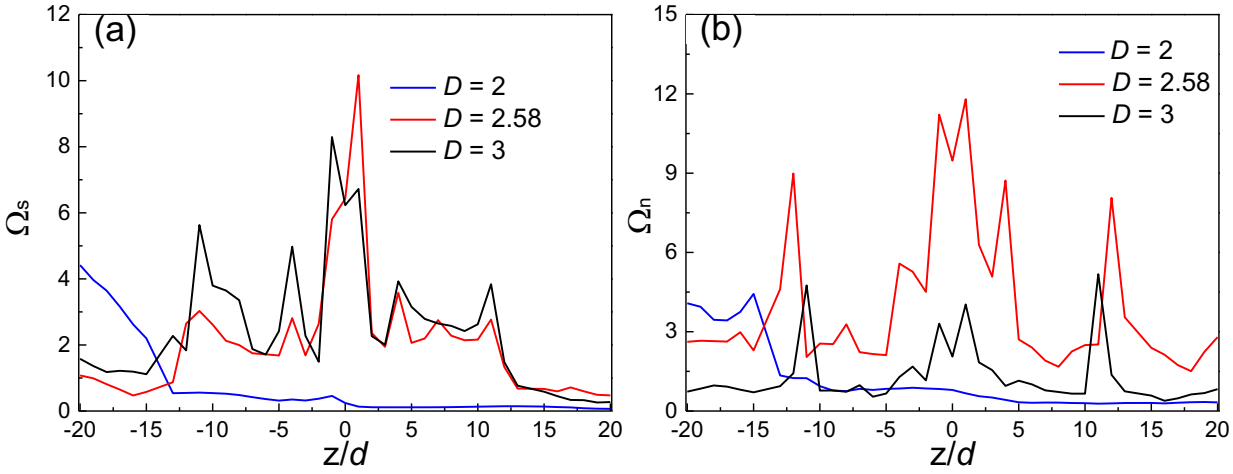

Fig. 15. Peak value variation of the normalized (a) streamwise vorticity Ω_s, and (b) spanwise vorticity Ω_n, for fractal injectors with different fractal dimensions (Q = 0.916 m^3/h, d_2 = 3 mm).

4.4 Mixing performance of the fractal injectors

The mixing effect can be examined by viewing the contours of the tracer mass fraction, w, and the isosurfaces of w = 0.5, which are given in Fig. 16 at t = 0.4 s and 0.8 s. The tracer mass fraction distribution for D = 2 is the least uniform, and a high concentration of tracer appears in the region near the bottom.

When D = 3, it is difficult for the tracer to diffuse, due to the weak turbulence and obstruction by the tube network. There are high tracer concentration regions in the jets' collision region, and dead zones under slice 3 and in between the tubes of the fractal injector. Among the three cases, the tracer can be most quickly distributed in the whole vessel when D = 2.58, and homogeneity can be achieved rapidly.

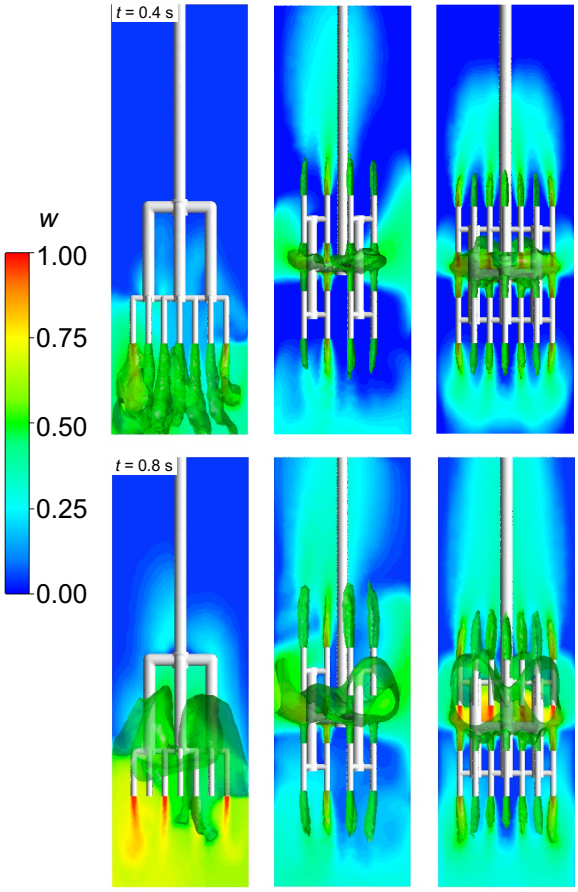

Fig. 16. The contour of the tracer mass fraction, w, and the isosurface of $w = 0.5$, represented for fractal injectors with (a) $D = 2$, (b) $D = 2.58$, and (c) $D = 3$ within vertical slice $y = 0$, at $t = 0.4$ s and 0.8 s ($Q = 0.916$ m^3/h, $d_2 = 3$ mm).

The macromixing performance can be quantitatively described by the standard deviation of the normalized mixing scalar, σ_w/w_{av} (Fig. 17). In the early stages of mixing, it can be observed that, among the three cases, σ_w/w_{av} is lowest for $D = 2$, which indicates that, in the initial stage, the turbulent flow near the jets plays a dominate role in mixing uniformity. Over time, however, at about $t = 0.175$ s, the curve for $D = 2.58$ intersects with the curve for $D = 2$, after which the injector with $D = 2.58$ leads to the lowest σ_w/w_{av}. This shows that the effect of the spatial distribution of the jet nozzles on mixing uniformity becomes significant. Although the nozzles are distributed spatially over the vessel in both cases $D = 2.58$ and 3, the local turbulence near the nozzles and the jet entrainment in the near field within the same fractal generating unit are stronger for $D = 2.58$, which results in a higher mass transfer rate, less accumulation and a more uniform tracer distribution.

The double toroidal vortices in $D = 3$ are mutually independent, so that the jet entrainment in the central region and mixing are not enhanced as much by the vortices as for $D = 2.58$.

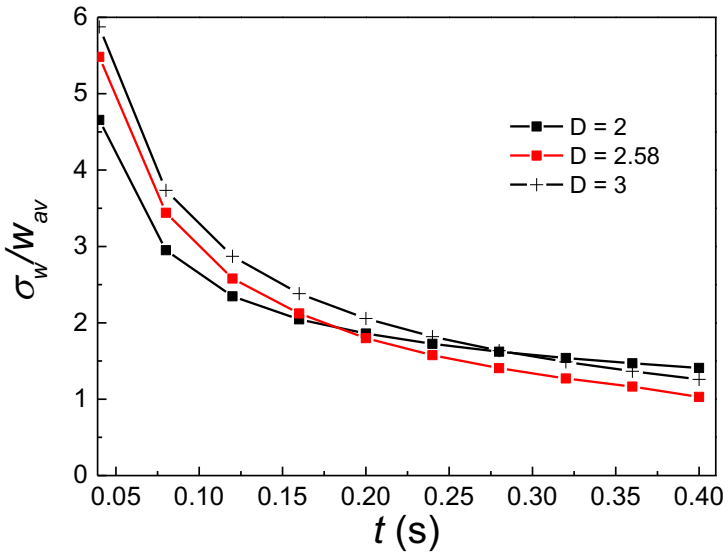

Fig. 17. Normalized standard deviation of the tracer mass fraction with mixing time, $\sigma_w/w_{av}\,(t)$ ($Q = 0.916$ m^3/h, $d_2 = 3$ mm).

We now turn our attention to the important problem of product selectivity for competing chemical reactions (Eqs. 10 and 11). This is illustrated in Fig. 18. The main reaction zone (MRZ) is defined as the zone where $C_C < C_{C0}$ (C being the slower reacting component, $CH_2ClCOOC_2H_5$), while the secondary reaction zone (SRZ) is defined as the zone where $C_B < C_{B0}$ (B being the faster reacting component, HCl). The remaining volume in the vessel is not affected by the competitive parallel reactions, so that $C_B = C_{B0} = 70$ mol/m^3 and $C_C = C_{C0} = 70$ mol/m^3. For $D = 2.58$, in the near-field region around the jets, close to the nozzles, the boundary of the SRZ extends much further than the MRZ, which is due to the intense turbulence near the shear layer, and the time scale of turbulent mixing is smaller. Further away from the nozzles, at the front of the jets, the degree of overlap between the two zones is relatively large. For $D = 3$, the MRZ and the SRZ have the least overlap. Since the injection velocity for $D = 3$ is the smallest among the three, and the diffusion of a component is controlled by molecular diffusion and turbulent diffusion, the characteristic mixing time is larger, so that the slow reaction is more likely to take place at the edge of the MRZ. For $D = 2$, the injection velocity is the

largest and, at the edge of the MRZ, the reactant A in the jets is more likely to diffuse with the jets and react with reactant B; therefore, the overall degree of overlap between these two zones is large.

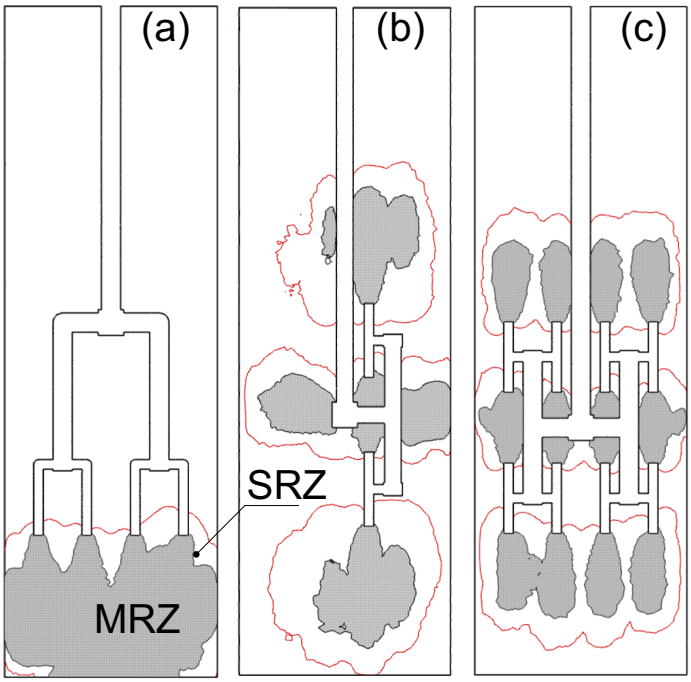

Fig. 18. Distribution of main reaction zones (MRZ, surrounded by the black curves) and secondary reaction zones (SRZ, surrounded by the red lines) within vertical slice $y = 0$, at $t = 0.05$ s ($Q = 0.916$ m^3/h, $d_2 = 3$ mm).

Fig. 19 presents the variation of the normalized volume of the turbulent mixing region in which the reactions occur, $\langle V_{eff} \rangle = V_{eff} / V_{total}$, where V_{eff} is the sum of the volumes of the regions affected by the competitive parallel reactions (volume of SRZ in Fig. 18). Initially, the curves for $D = 2$ and 3 overlap, whilst later, at $t = 0.02$ s, $\langle V_{eff} \rangle$ for $D = 3$ already exceeds that for $D = 2$. It can be observed that, at $t = 0.03$ s, the growth rate of the effective reaction volume of $D = 2$ begins to slow down. At the initial stage of injection, for $D = 2$, because of the high injection velocity, the turbulence around the nozzles is strong, the reactions proceed, and the reactants in the area around the nozzles are rapidly consumed. Since the flow in this region is so fast, it takes a certain distance for the jets to develop and continue the reactions. For $D = 2.58$, due to the relatively high injection velocity and the spatial distribution of the nozzles, which can efficiently make use of the volume in the vessel, the growth rate of the reaction volume is the highest and is maintained for the entire observation period. This characteristic to carry out a reaction in the whole vessel quickly and selectively is highly

significant for the application of the fractal injector with intermediate fractal dimension (D = 2.58) in rapid reaction processes, where the scalability of the injector, thanks to its self-similar structure, should be an additional advantage.

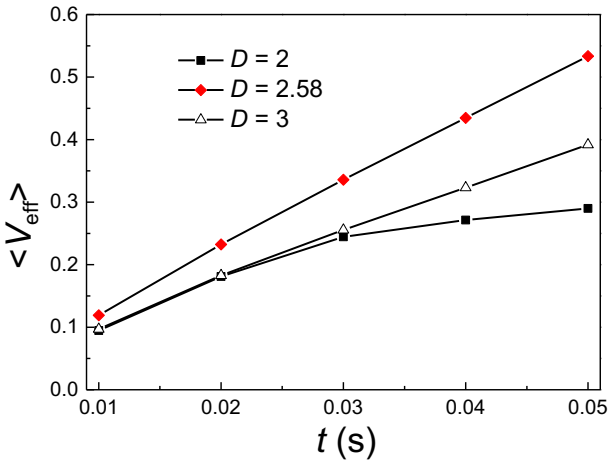

Fig. 19. Normalized effective reaction volume, $<V_{eff}>$ as a function of mixing time, t (Q = 0.916 m^3/h, d_2 = 3 mm).

5. Conclusion

In the present work, the flow field characteristics and turbulent mixing process for a vessel equipped with a fractal injector have been investigated using CFD simulations. The RNG k-ε turbulence model, validated by PIV data, was used to predict the flow field. An injector of intermediate fractal dimension, D = 2.58, was compared with injectors with D = 2 (all nozzles in a single plane) and 3 (space-filling, with nozzles distributed over a three-dimensional volume).

The flow field of a fractal injector with D = 2.58 contains two characteristic types of vortices: single spiral vortices and double toroidal vortices. The former mainly distribute fluid in the region near the nozzles located at the uppermost and downmost layers, which mostly interact with ambient fluids. The jets injected from the nozzles of the downmost layer reach the bottom, and then form a large-scale wall vortex structure. The double toroidal vortices mainly occur in the region where two jets impact each other. When adjacent pairs of double toroidal vortices interact, the flow field becomes non-axisymmetric.

On this basis, a comparison between the flow fields of fractal injectors with different configurations and fractal dimensions has been carried out. For D = 2, there are only multiple jets impinging on the wall, the decaying trends of the spanwise and streamwise vorticity profiles are basically the same, and the peak value of the spanwise vorticity is lower than the streamwise vorticity. The nozzles of D = 2 are all distributed within one horizontal plane and the vessel volume cannot be made fully use of, so, although mixing is fast near the nozzles, D = 2 can only achieve mixing uniformity in the bottom half of the vessel.

For D = 2.58 and D = 3, the profiles of the streamwise vorticity are basically the same. However, for D = 2.58, the vorticity of the spanwise vortices is larger than that for D = 3, and its distribution is strongly affected by the arrangement of the nozzles. An interesting point to note here is that, although D = 3 has a denser spatial distribution of nozzles than D = 2.58, the mixing behavior is not as good as one might have expected. This could be explained by the mutually independent double toroidal vortex pairs and the weak turbulent mixing for D = 3. In the case of D = 2.58, due to the strong interaction between local turbulent mixing around every nozzle, a high mixing rate is obtained, as well as the most uniform concentration distribution, leading to the ability to carry out a reaction in the whole vessel quickly and selectively, as the tracer distribution and reaction simulations demonstrate.

The results suggest the possibility to utilize fractal injectors of intermediate, optimized fractal dimension and other characteristics, such as the shape and the relative positions of fractal generating units, to intensify processes that rely on well controlled liquid-liquid mixing. In addition, the scalability of the fluid dynamics thanks to self-similarity of the injectors is a clear benefit for manufacturing. These aspects will be explored in future work.

Declaration of interests

The authors declare no conflicts of interest.

Acknowledgments

This work was financially supported by the National Key R&D Program of China (2017YFB0307702), the National Nature Science Foundation of China (22078284) and the State Key Laboratory of Chemical Engineering (SKL-ChE-16D02). M.-O. C. is grateful to EPSRC for a “Frontier Engineering” (EP/K038656/1)

and “Frontier Engineering: Progression” (EP/S03305X/1) Awards at UCL, as well as to Zhejiang University for a Qiushi Chair Professorship, funding his stays at Zhejiang University and making this collaboration possible.

References

Baldyga, J., Bourne, J.R., 1984. A fluid mechanical approach to turbulent mixing and chemical reaction part iii computational and experimental results for the new micromixing model. Chem. Eng. Commun. 28, 259-281.
Bałdyga, J., Pohorecki, R., 1995. Turbulent micromixing in chemical reactors—a review. Chem. Eng. J. Biochem. Eng. J. 58, 183-195.
Basbug, S., Papadakis, G., Vassilicos, J.C., 2018. Reduced power consumption in stirred vessels by means of fractal impellers. AIChE J. 64, 1485-1499.
Bejan, A., 2000. Shape and structure, from engineering to nature. Cambridge University Press.
Bernal, L., Roshko, A., 1986. Streamwise vortex structure in plane mixing layers. J. Fluid Mech. 170, 499-525.
Cafiero, G., Discetti, S., Astarita, T., 2014. Heat transfer enhancement of impinging jets with fractal-generated turbulence. Int. J. Heat Mass Tran. 75, 173-183.
Cafiero, G., Discetti, S., Astarita, T., 2015. Flow field topology of submerged jets with fractal generated turbulence. Phys. Fluids 27, 115103.
Cafiero, G., Greco, C.S., Astarita, T., Discetti, S., 2016. Flow field features of fractal impinging jets at short nozzle to plate distances. Exp. Therm. Fluid Sci. 78, 334-344.
Christensen, D., Nijenhuis, J., van Ommen, J., Coppens, M.-O., 2008a. Influence of distributed secondary gas injection on the performance of a bubbling fluidized-bed reactor. Ind. Eng. Chem. Res. 47, 3601-3618.
Christensen, D., Nijenhuis, J., Van Ommen, J.R., Coppens, M.O., 2008b. Residence times in fluidized beds with secondary gas injection. Powder Technol. 180, 321-331.
Coppens, M.-O., 2001. Method for operating a chemical and/or physical process by means of a hierarchical fluid injection system. U.S. Patent 6,333,019.
Coppens, M.-O., 2005. Scaling-up and -down in a nature-inspired way. Ind. Eng. Chem. Res. 44, 5011-5019.
Coppens, M.-O., Cheng, Y., Van den Bleek, C.M., 1999. Controlling fluidized bed operation using a novel hierarchical gas injection system. American Institute of Chemical Engineers.
Coppens, M.-O., Froment, G.F., 1995. Diffusion and reaction in a fractal catalyst pore—i. Geometrical aspects. Chem. Eng. Sci. 50, 1013-1026.
Coppens, M.-O., van Ommen, J.R., 2003. Structuring chaotic fluidized beds. Chem. Eng. J. 96, 117-124.
Geipel, P., Goh, K.H.H., Lindstedt, R.P., 2010. Fractal-generated turbulence in opposed jet flows. Flow Turbul. Combust. 85, 397-419.

Han, Y., Wang, J.-J., Gu, X.-P., Feng, L.-F., 2012. Numerical simulation on micromixing of viscous fluids in a stirred-tank reactor. Chem. Eng. Sci. 74, 9-17.
Hu, H., Saga, T., Kobayashi, T., Taniguchi, N., 2002. Mixing process in a lobed jet flow. AIAA J. 40, 1339-1345.
Jiang, S., Wang, J., Feng, L.-F., Coppens, M.-O., 2020. Hydrodynamics and local turbulent mixing of submerged, parallel liquid jets: Experiments and cfd simulations. Ind. Eng. Chem. Res. 59, 3985-3995.
Kearney, M.M., 1999. Fractal cascade as an alternative to inter-fluid turbulence. US. Patent 5938333.
Kearney, M.M., 2000. Engineered fractals enhance process applications. Chem. Eng. Prog. 96, 61-68.
Kjelstrup, S., Coppens, M.-O., Pharoah, J.G., Pfeifer, P., 2010. Nature-inspired energy- and material-efficient design of a polymer electrolyte membrane fuel cell. Energy Fuels 24, 5097-5108.
Kockmann, N., Föll, C., Woias, P., 2003. Flow regimes and mass transfer characteristics in static micromixers, Microfluidics, BioMEMS, and Medical Microsystems. International Society for Optics and Photonics, pp. 319-329.
Lasheras, J.C., Cho, J.S., Maxworthy, T., 1986. On the origin and evolution of streamwise vortical structures in a plane, free shear layer. J. Fluid Mech. 172, 231-258.
Li, Z., Bao, Y., Gao, Z., 2011. Piv experiments and large eddy simulations of single-loop flow fields in rushton turbine stirred tanks. Chem. Eng. Sci. 66, 1219-1231.
Liepmann, D., Gharib, M., 1992. The role of streamwise vorticity in the near-field entrainment of round jets. J. Fluid Mech. 245, 643-668.
Luo, L., Fan, Z., Le Gall, H., Zhou, X., Yuan, W., 2008. Experimental study of constructal distributor for flow equidistribution in a mini crossflow heat exchanger (mche). Chem. Eng. Process 47, 229-236.
Luo, P., Fang, Y., Wu, B., Wu, H., 2016. Turbulent characteristics and design of transverse jet mixers with multiple orifices. Ind. Eng. Chem. Res. 55, 8858-8868.
Mandelbrot, B.B., 1983. The fractal geometry of nature. WH freeman New York.
Nagata, K., Sakai, Y., Inaba, T., Suzuki, H., Terashima, O., Suzuki, H., 2013. Turbulence structure and turbulence kinetic energy transport in multiscale/fractal-generated turbulence. Phys. Fluids 25, 065102.
Nedic, J., Ganapathisubramani, B., Vassilicos, J.C., Boree, J., Brizzi, L.E., Spohn, A., 2012. Aeroacoustic performance of fractal spoilers. AIAA J. 50, 2695-2710.
Schwertfirm, F., Gradl, J., Schwarzer, H.C., Peukert, W., Manhart, M., 2007. The low reynolds number turbulent flow and mixing in a confined impinging jet reactor. Int J Heat Fluid Flow 28, 1429-1442.
Steiros, K., Bruce, P.J., Buxton, O.R., Vassilicos, 2017. Power consumption and form drag of regular and fractal‐shaped turbines in a stirred tank. AIChE J. 63, 843-854.
Tondeur, D., Luo, L., 2004. Design and scaling laws of ramified fluid distributors by the constructal approach. Chem. Eng. Sci. 59, 1799-1813.
Toyoda, K., Hiramoto, R., 2006. Effect of streamwise vortices on characteristics of

jets. JSME Int. J. Ser. B Fluids Therm. Eng. 49, 884-889.
Trogadas, P., Cho, J.I.S., Neville, T.P., Marquis, J., Wu, B., Brett, D.J.L., Coppens, M.O., 2018. A lung-inspired approach to scalable and robust fuel cell design. Energy Environ. Sci. 11, 136-143.
Trogadas, P., Coppens, M.-O., 2020. Nature-inspired electrocatalysts and devices for energy conversion. Chem. Soc. Rev. 49, 3107-3141.
Van Ommen, J.R., Schouten, J.C., Coppens, M.O., Van den Bleek, C.M., 2001. Monitoring fluidized bed hydrodynamics to detect changes in particle size distribution, 10th Engineering Foundation Conf. on Fluidization (Fluidization X). United Engineering Foundation, UEF New York, pp. 787-794.
van Willigen, F.K., Christensen, D., Van Ommen, J., Coppens, M.-O., 2005. Imposing dynamic structures on fluidised beds. Catal. Today 105, 560-568.
Weitemeyer, S., Reinke, N., Peinke, J., Holling, M., 2013. Multi-scale generation of turbulence with fractal grids and an active grid. Fluid Dyn. Res. 45, 061407.
Xu, K., Wang, G., Wang, L., Yun, F., Sun, W., Wang, X., Chen, X., 2020. Cfd-based study of nozzle section geometry effects on the performance of an annular multi-nozzle jet pump. Processes 8, 133.
Yakhot, V., Orszag, S.A., Thangam, S., Gatski, T.B., Speziale, C.G., 1992. Development of turbulence models for shear flows by a double expansion technique. Phys. Fluids A 4, 1510-1520.
Yu, S., 1993. Micromixing and parallel reactions, Ph.D. Thesis. Swiss Federal Inst. Of Tech., Zurich.
Zhou, Y., Nagata, K., Sakai, Y., Suzuki, H., Ito, Y., Terashima, O., Hayase, T., 2014. Relevance of turbulence behind the single square grid to turbulence generated by regular- and multiscale-grids. Phys. Fluids 26, 075105.